Unmixing biogenic and terrigenous magnetic mineral components in red clay of the Pacific Ocean using principal component analyses of first-order reversal curve diagrams and paleoenvironmental implications

FULL PAPER

Unmixing biogenic and terrigenous magnetic mineral components in red clay of the Pacific Ocean using principal component analyses of first-order reversal curve diagrams and paleoenvironmental implications

Toshitsugu Yamazaki[1*] , Wei Fu[1], Takaya Shimono[2] and Yoichi Usui[3]

Abstract

Red clay widely occupies the seafloor of pelagic environments in middle latitudes, and potentially preserves long paleoceanographic records. We conducted a rock-magnetic study of Pacific Ocean red clay to elucidate paleoenvironmental changes. Three piston cores from the western North Pacific Ocean and IODP Hole U1365A cores in the South Pacific Ocean were studied here. Principal component analyses applied to first-order reversal curve diagrams (FORC-PCA) reveals three magnetic components (endmembers EM1 through EM3) in a core of the western North Pacific. EM1, which represents the features of interacting single-domain (SD) and vortex states, is interpreted to be of terrigenous origin. EM2 and EM3 are carried by non-interacting SD grains with different coercivity distributions, which are interpreted to be of biogenic origin. The EM1 contribution suddenly increases upcore at a depth of ~ 2.7 m, which indicates increased eolian dust input. The age of this event is estimated to be around the Eocene–Oligocene (E/O) boundary. Transmission electron microscopy reveals that EM2 is dominated by magnetofossils with equant octahedral morphology, while EM3 has a higher proportion of bullet-shaped magnetofossils. An increased EM3 contribution from ~ 6.7 to 8.2 m suggests that the sediments were in the oxic–anoxic transition zone (OATZ), although the core is oxidized in its entire depth now. The chemical conditions of OATZ may have been caused by higher biogenic productivity near the equator. FORC-PCA of Hole U1365A cores identified two EMs, terrigenous (EM1) and biogenic (EM2). The coercivity distribution of the biogenic component at Hole U1365A is similar to that of the lower coercivity biogenic component in the western North Pacific. A sudden upcore terrigenous-component increase is also evident at Hole U1365A with an estimated age around the E/O boundary. The increased terrigenous component may have been caused by the gradual tectonic drift of the sites on the lee of arid continental regions in Asia and Australia, respectively. Alternatively, the eolian increase may have been coeval in the both hemispheres and associated with the global cooling at the E/O boundary.

Keywords: Red clay, Rock magnetism, FORC diagram, Biogenic magnetite, Eolian dust, Eocene–Oligocene boundary

Introduction

Red clay occurs widely in mid-latitude seafloor below the carbonate compensation depth. It covers ~ 40% of the Pacific Ocean seafloor. Red clay contains almost no calcareous or siliceous microfossils, which makes it difficult to estimate precise sediment ages. Furthermore,

*Correspondence: yamazaki@aori.u-tokyo.ac.jp
[1] Atmosphere and Ocean Research Institute, The University of Tokyo, Kashiwa, Japan
Full list of author information is available at the end of the article

Yamazaki *et al. Earth, Planets and Space*   (2020) 72:120

Page 2 of 15

deposition rates are extremely low, a few meters per million years or less, and hiatuses can occur (e.g., Opdyke and Foster 1970). These drawbacks hinder high-resolution paleoceanographic studies. However, the slow sedimentation of red clay provides the possibility to study environmental changes over long time spans (Janecek and Rea 1983; Dunlea et al. 2015; Shimono and Yamazaki 2016; Nozaki et al. 2019; Ohta et al. 2020); an ordinary ~ 10 m piston core may reach sediment ages of tens of millions of years ago.

The major source of pelagic red clay is considered to be eolian dust transported from arid continental regions (e.g., Rex and Goldberg 1958; Rea 1994). Thus, red clay can preserve records of continental environments and atmospheric circulation. For example, sedimentological studies of red clay reveal increased eolian flux and grain size in conjunction with the onset of northern hemisphere glaciation (Janecek and Rea 1983) and fluctuating eolian fluxes since the middle Pleistocene associated with glacial–interglacial cycles (Hovan et al. 1991). Recently, red clay has also attracted interest as a potential source of rare-earth elements and yttrium (REY). Layers with high REY concentrations occur widely in red clay provinces (Kato et al. 2011; Iijima et al. 2016; Tanaka et al. 2020; Ohta et al. 2020).

Environmental magnetism can provide records of the processes that generate, transport, deposit, and alter sediments using rock-magnetic techniques (e.g., Thompson and Oldfield 1986; Liu et al. 2012). Environmental magnetism can be particularly useful for studying red clay, because the lack of calcareous and siliceous microfossils hinders use of geochemical and paleontological methods that are generally used in paleoceanographic research. In previous environmental magnetic studies of red clay, the concentration of high-coercivity magnetic minerals such as hematite and goethite was used as an eolian flux indicator, and eolian grain-size variations were estimated from rock-magnetic proxies of magnetic mineral grain size (Doh et al. 1988; Yamazaki and Ioka 1997; Shimono and Yamazaki 2016; Zhang et al. 2018).

It has become recognized that fossil biogenic magnetites (magnetofossils) have widespread occurrence in marine sediments (Roberts et al. 2011, 2012, 2013; Yamazaki and Ikehara 2012; Yamazaki and Shimono 2013; Yamazaki and Horiuchi 2016; Zhang et al. 2018). It is considered that magnetotactic bacteria are microaerophilic or anaerobic and prefer chemical conditions in the oxic-anoxic transition zone (OATZ) in a sediment or water column (Blakemore et al. 1979; Bazylinski and Frankel 2004; Lefèvre and Bazylinski 2013). Red clays are oxic sediments devoid of an OATZ (D'Hondt et al. 2015), and thus it is not expected to yield biogenic magnetites. However, it has been revealed that biogenic magnetites

are the major constituent of magnetic mineral assemblages in red clay (Yamazaki and Shimono 2013; Shimono and Yamazaki 2016; Usui et al. 2017). Usui et al. (2017) reported variations in the dominant magnetofossil morphology within a red clay core from the western North Pacific Ocean based mainly on analysis of isothermal remanent magnetization (IRM) acquisition curves and transmission electron microscope (TEM) observations.

We conducted an environmental magnetic study of red-clay cores from the western North Pacific and South Pacific Oceans. Sediments usually contain a mixture of magnetic minerals in various domain states and arrangements. First-order reversal curve (FORC) diagrams (Pike et al. 1999; Roberts et al. 2000) have become widely recognized as a robust and quantitative method to evaluate the constituents of magnetic mineral assemblages (e.g., Muxworthy et al. 2005; Roberts et al. 2014). We apply principal component analysis (PCA) to a set of FORC diagrams (Lascu et al. 2015; Harrison et al. 2018) to unmix magnetic components. Combined with other rock-magnetic proxies and TEM observations, we discuss the paleoceanographic implications of the magnetic components identified in terms of eolian dust and biogenic magnetite variations.

Samples

Western North Pacific Ocean

About 50 sediment cores were taken with a piston corer around Minamitorishima Island in the western North Pacific Ocean under a research project of the Japan Agency for Marine-Earth Science and Technology (JAMSTEC) (Fujinaga et al. 2016; Iijima et al. 2016; Tanaka et al. 2020). Three cores were selected for this study: core PC06 taken during the R/V *Kairei* KR13-02 cruise, core PC01 of the R/V *Mirai* cruise MR13-E02 Leg 2, and core PC04 of the R/V *Kairei* KR14-02 cruise (Fig. 1). The positions, water depths, and lengths of these cores are listed in Table 1. The cores consist of brown, dark brown, and blackish-brown pelagic clay. Core KR13-02 PC06 has particularly dark color between ~ 1.5 and 6.7 m, while it has brown and yellowish brown alternations below ~ 6.8 m. The brownish colors indicate that at present the sediments are in oxidized conditions throughout the cores, and that no OATZ occurs. Core photos are provided in Additional file 1: Fig. S1, and visual core descriptions are available at the Data and Sample Research System for Whole Cruise Information (DARWIN) (2020) of JAMSTEC.

A typical red clay section in this area was established from lithology and geochemistry, and sediments from individual cores are divided into chemostratigraphical Units (Tanaka et al. 2020) (Fig. 2). Although precise ages have not yet been obtained because of the lack of
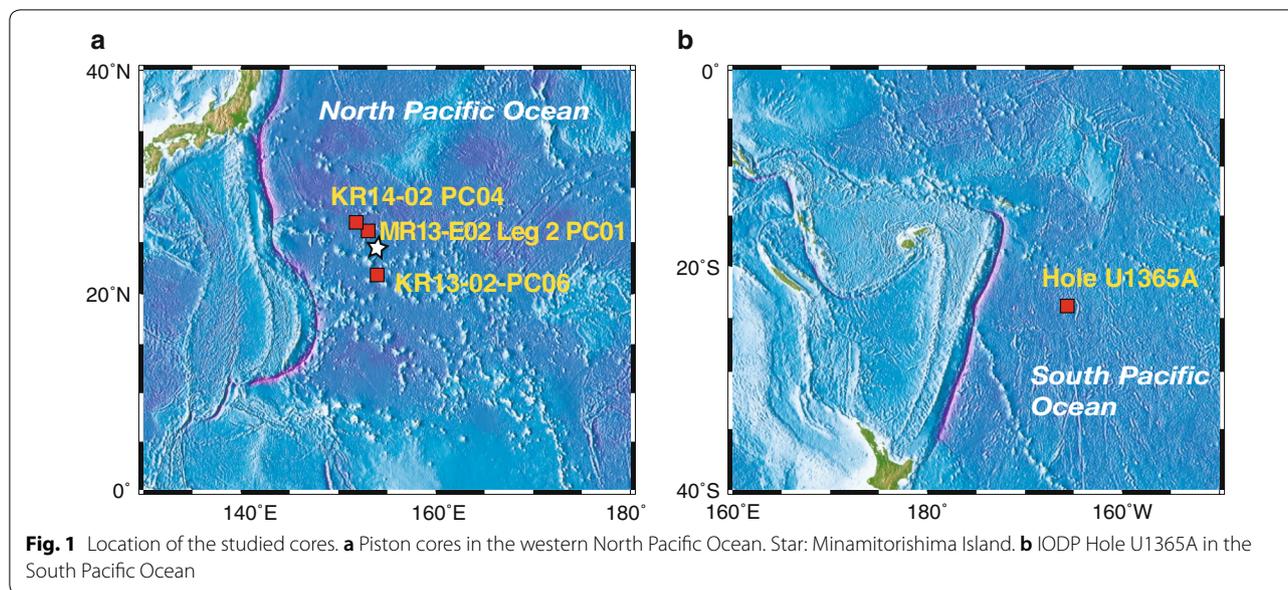
Fig. 1 Location of the studied cores. **a** Piston cores in the western North Pacific Ocean. Star: Minamitorishima Island. **b** IODP Hole U1365A in the South Pacific Ocean

Table 1 Position, water depth, and core lengths of the studied cores in the western North Pacific Ocean

Core ID	Latitude	Longitude	Water depths (m)	Core length (m)
KR13-02 PC06	21°51.01′ N	153° 59.98′ E	5755	11.68
MR13-E02 Leg 2 PC01	26°04.19′ N	153° 04.01′ E	5936	12.90
KR14-02 PC04	26° 49.95′ N	151° 48.70′ E	6031	4.43

calcareous and siliceous microfossils, the age of each unit could be estimated roughly. Core MR13-E02 Leg 2 PC01 consists of Unit I, which is estimated to be of Quaternary age from magnetostratigraphy (Additional file 1: Fig. S2). Core KR14-02 PC04 reaches Unit II. A sequence of magnetic polarity flips was recovered from this core, but it is difficult to correlate the polarity sequence to the geomagnetic polarity time scale (Additional file 1: Fig. S3). Core KR13-02 PC06 has a thin Unit I and reaches Unit V. Ohta et al. (2020) reported an age model for nearby core KR13-02 PC05 based on osmium (Os) isotope ratios. According to the age model, the age of the first layer of high REY content would be near the Eocene–Oligocene (E/O) boundary. Intercore correlation between core KR13-02 PC05 and PC06 based on REY contents and chemostratigraphy (Fig. 2) suggests that Unit II is Oligocene to Miocene in age and its lowest part would be near the E/O boundary, although this part is not marked as the "1st ΣREY peak" in Tanaka et al. (2020), because the REY content is below their threshold as a REY-rich layer.

South Pacific Ocean

We also studied cores from Integrated Ocean Drilling Program (IODP) Hole U1365A (Lat. 23° 51.00′ S, Lon.

165° 38.70′ W) (Fig. 1). Hole U1365A is located at the western edge of the South Pacific Gyre. Red clay cores of 75.5 m length accumulated above basaltic basement with ~125.5 Ma age were recovered with an advanced piston corer (Expedition 329 Scientists 2011). Magnetostratigraphy was established only above ~6 m in depth, which spans the last ~5 m.y. (Shimono and Yamazaki 2016). The Os-isotope age model of red-clay cores from Deep Sea Drilling Project (DSDP) Hole 596 (Ohta et al. 2020), which is located ~400 km west of Hole U1365A, and intercore correlation between Holes U1365A and 596 using magnetic susceptibility suggests ages around the E/O boundary for Hole U1365A sediments from ~7.4 to 9 m (Additional file 1: Fig. S4).

Methods
FORC diagram

FORC diagrams map the distributions of coercivity (H_c) and magnetostatic interactions (H_u) for the magnetic particle assemblage in a sample, from which information on domain states, grain sizes and shapes, mineralogy, and spatial distribution of the constituents can be obtained (Pike et al. 1999; Roberts et al. 2000, 2014). FORC diagrams are particularly useful for detecting biogenic
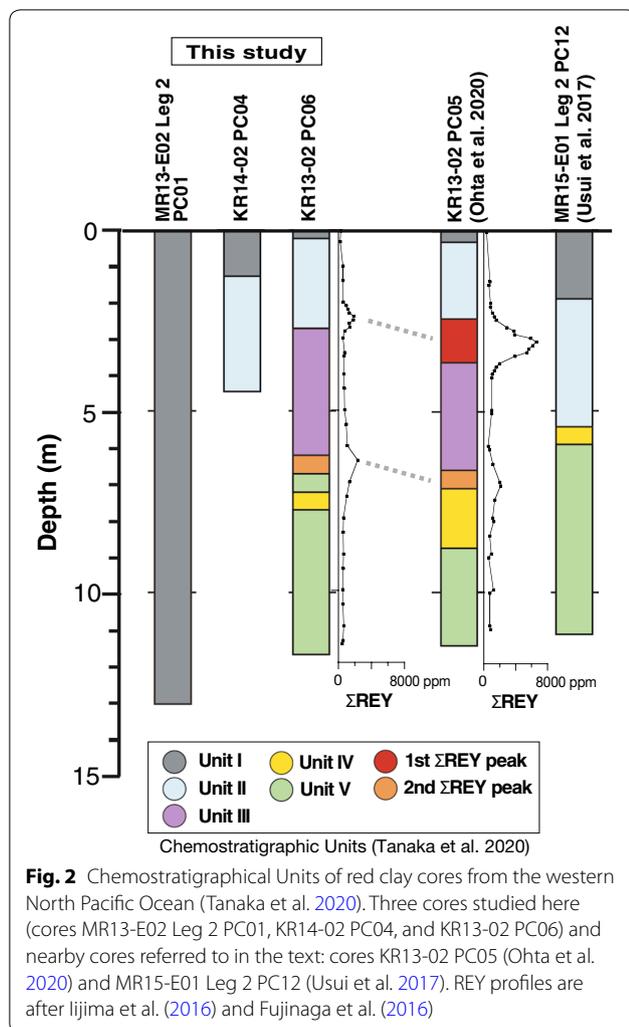
Yamazaki *et al. Earth, Planets and Space* (2020) 72:120

Page 4 of 15

Fig. 2 Chemostratigraphical Units of red clay cores from the western North Pacific Ocean (Tanaka et al. 2020). Three cores studied here (cores MR13-E02 Leg 2 PC01, KR14-02 PC04, and KR13-02 PC06) and nearby cores referred to in the text: cores KR13-02 PC05 (Ohta et al. 2020) and MR15-E01 Leg 2 PC12 (Usui et al. 2017). REY profiles are after Iijima et al. (2016) and Fujinaga et al. (2016)

magnetite in sediments. A narrow peak elongated along the coercivity axis at zero interaction field ($H_u = 0$), called the "central ridge", is considered to be diagnostic of intact chains of biogenic magnetites in sediments (Chen et al. 2007; Yamazaki 2008; Egli et al. 2010; Li et al. 2012; Roberts et al. 2012; Chang et al. 2014).

FORC measurements were conducted using alternating-gradient magnetometers (Princeton MicroMag 2900) at the Atmosphere and Ocean Research Institute (AORI), The University of Tokyo, and the Geological Survey of Japan (GSJ), National Institute of Advanced Industrial Science and Technology (AIST). Dried samples were cut to suitable sizes (tens of milligrams) and leave stuck to a probe with silicon grease. For samples of core KR13-E02 PC06 (26 samples) and Hole U1365A (30 samples, partly presented by Yamazaki and Shimono (2013) and Shimono and Yamazaki (2016)), a total of 231 FORCs (191 FORCs for Hole U1365A) were measured, with H_c between 0 and 80 mT (60 mT for Hole U1365A), H_u between -15 and

15 mT, and field spacing of 0.5 mT. The maximum applied field was 1.0 T, and the averaging time for each measurement point was 200 ms. For samples from cores MR13-E02 Leg 2 PC01 ($n = 9$) and KR14-02 PC04 ($n = 7$), 150 FORCs were measured, with H_c between 0 and 100 mT, H_u between -50 and 50 mT, and field spacing of 1.3 mT.

Application of PCA to a set of FORC diagrams (FORC-PCA) was introduced by Lascu et al. (2015) and improved by Harrison et al. (2018) as a quantitative method to unmix a suite of FORC distributions into a linear combination of endmembers (EMs). It has become a powerful tool in environmental magnetic studies (Channell et al. 2016; Roberts et al. 2018). The FORCinel software (Harrison and Feinberg 2008, version 3.05 in 2019) was used for the analyses, and the VARIFORC algorithm of Egli (2013) was used for smoothing ($S_{c0} = 4$, $S_{b0} = 3$, $S_{c1} = S_{b1} = 7$), which provides smaller smoothing in regions near $H_u = 0$ and for areas with low coercivities and larger smoothing for other regions. EMs can be visualized and selected interactively using FORCinel. The contribution of each EM to the total magnetization is completely independent. EM selection is not physically constrained, so we need to choose rock-magnetically realistic EMs.

Ratio of ARM to SIRM

The ratio of anhysteretic remanent magnetization (ARM) susceptibility (k_{ARM}) to saturation IRM (SIRM) is often used as a proxy for magnetic grain-size variations, and the k_{ARM}/SIRM ratio decreases with increasing average magnetic grain size (Banerjee et al. 1981; King et al. 1982). k_{ARM}/SIRM is also sensitive to the relative abundance of biogenic magnetite and terrigenous magnetic minerals (Egli 2004a; Yamazaki 2008). This is because the acquisition of ARM is sensitive to magnetostatic interactions among magnetic grains (higher efficiency for smaller interactions) and magnetostatic interactions among individual chains of biogenic magnetites are expected to be negligibly small; a chain of biogenic magnetites behaves as a single elongated uniaxial particle. In pelagic environments, where grain-size variations of sediments are expected to be small, k_{ARM}/SIRM is considered to reflect mainly the relative abundance of terrigenous magnetic minerals with stronger magnetostatic interactions to biogenic magnetite with little interactions (Yamazaki et al. 2013; Shimono and Yamazaki 2016).

k_{ARM}/SIRM was measured for the studied cores from the western North Pacific Ocean. After natural remanent magnetization measurements, an ARM was imparted with a peak alternating field of 80 mT and a direct-current (DC) bias field of 0.1 mT to samples using cryogenic magnetometer systems (2G Enterprises model 760) at the GSJ and the Center for Advanced Marine Core Research, Kochi University. k_{ARM} was calculated by normalizing the

Yamazaki *et al. Earth, Planets and Space*   (2020) 72:120

Page 5 of 15

measured ARM intensity by the strength of the DC field. An IRM was imparted in a 2.5 T inducing field using pulse magnetizers (2G Enterprises model 660 at GSJ and Magnetic Measurements MMPM-10 at AORI). Here the IRM acquired in a 2.5 T field is regarded as SIRM. The IRMs were measured using spinner magnetometers (Natsuhara-Giken SMM-85 at GSJ and Natsuhara-Giken A-Spin at AORI).

TEM observations

Although FORC-PCA is a quantitative method, it still only provides an indirect way to detect magnetic mineral composition in sediments. Using a TEM, we can confirm the occurrence of biogenic magnetite from their characteristic morphologies (octahedron, hexagonal prism, and bullet shape) and grain sizes, which are restricted within the narrow single-domain (SD) range (tens of nanometers) (Kopp and Kirschvink 2008).

Magnetic minerals extracted from core KR13-02 PC06 were observed using a TEM. To extract magnetic minerals, sediments were first dispersed in distilled water with sodium hexametaphosphate using an ultrasonic bath, and magnetic minerals were collected by circulating the dispersed sediments through a high magnetic-field gradient. The magnetic extracts were dispersed in ethanol, and a small drop of the suspension was subsequently dried on a carbon-coated copper grid. A TEM (JEOL JEM-1400) at AORI, operated at 120 kV, was used for the observations. From morphologies observed in TEM images, magnetofossils were classified into three groups: bullet shape, elongated, and equant. The elongated group consists mainly of hexagonal prisms and elongated octahedra. The equant group is represented by cubo-octahedra, although short hexagonal prisms with length/width ratios close to one are also included in this group. About one hundred grains were counted for each sample.

Results

Core KR13-02 PC06, western North Pacific Ocean

FORC diagrams for core KR13-02 PC06 samples consist of a central ridge and a broader component with large vertical spread, which has outer contours that diverge from the $H_u=0$ line (Fig. 3). The central ridge component represents a population of non-interacting SD grains. The broad component is considered to be carried by a mixture of SD grains with strong magnetostatic interactions and grains in a vortex state. The broad component becomes small below ~2.7 m in the core.

The results of FORC-PCA applied to 26 samples are shown in Fig. 4a, in which squares represent PCA scores for individual samples on the principal component PC1-PC2 plane. Data variance of ~87% can be explained by the two PCs. The triangular region on this plane (dashed

lines) defines a three-EM system. The three EMs were selected manually. The arrow indicates a general downcore trend. FORC diagrams of the three EMs are shown in Fig. 4b. EM1 has an elliptical peak centered at $H_c=$ ~15 mT on the $H_u=0$ axis with significant vertical spread, and does not contain a central ridge. EM1 represents the component carried by interacting SD/vortex grains. We interpret this endmember as a terrigenous magnetic component consisting of aggregated SD grains and/or grains larger than SD. This may also include collapsed chains of biogenic magnetite (Li et al. 2012; Harrison and Lascu 2014). EM2 and EM3 have a central ridge and a small negative region near the vertical (H_u) axis below zero, which represents the non-interacting SD component (Muxworthy et al. 2004; Newell 2005; Egli et al. 2010). The coercivity distribution of EM2 has a peak at ~15 mT and tails to ~60 mT, and that of EM3 has a peak at ~30 mT and tails to >80 mT. We interpret these two EMs to represent intact biogenic magnetite chains with different coercivity distributions.

Downcore variations in the proportion of the three EMs and the magnetizations carried by them, which were calculated from SIRM and the respective EM proportions, are shown in Fig. 5 with k_{ARM}/SIRM variations. Note that the measured FORC coercivity range of the EMs is from 0 to 80 mT; components with coercivity > 80 mT (generally 10% or less of the total magnetization) may not be represented by these EMs. The terrigenous component (EM1) contribution suddenly increases upcore at ~2.7 m, whereas the magnetizations carried by the biogenic components (EM2 and EM3) do not change much. The terrigenous component becomes dominant (>70%) above ~2.7 m, which is synchronous with a large k_{ARM}/SIRM decrease. An increased EM1 proportion between ~5 and 6.7 m also accompanies a k_{ARM}/SIRM decrease. These observations confirm that k_{ARM}/SIRM is sensitive to changes in the proportion of terrigenous to biogenic magnetic components. k_{ARM}/SIRM values between ~2.7 and 4.5 m and below ~6.5 m, which ranges from ~2.5 to 3×10^{-3} m/A, are the highest among reported values for various Pacific deep-sea sediments (Yamazaki et al. 2013; Sakuramoto et al. 2017; Yamazaki and Yamamoto 2018). About 70% or more of SIRM is carried by biogenic magnetite in these intervals. The proportion of the higher coercivity biogenic component (EM3) increases significantly from ~20 to 60% within an interval from ~6.7 to 8.2. SIRM also increases significantly in this interval. The SIRM increase is due mainly to the increased EM3 contribution, although EM1 also increases somewhat in this interval.

To understand the different coercivity distributions of EM2 and EM3, magnetic minerals extracted from the sediments were observed with a TEM. Magnetofossils
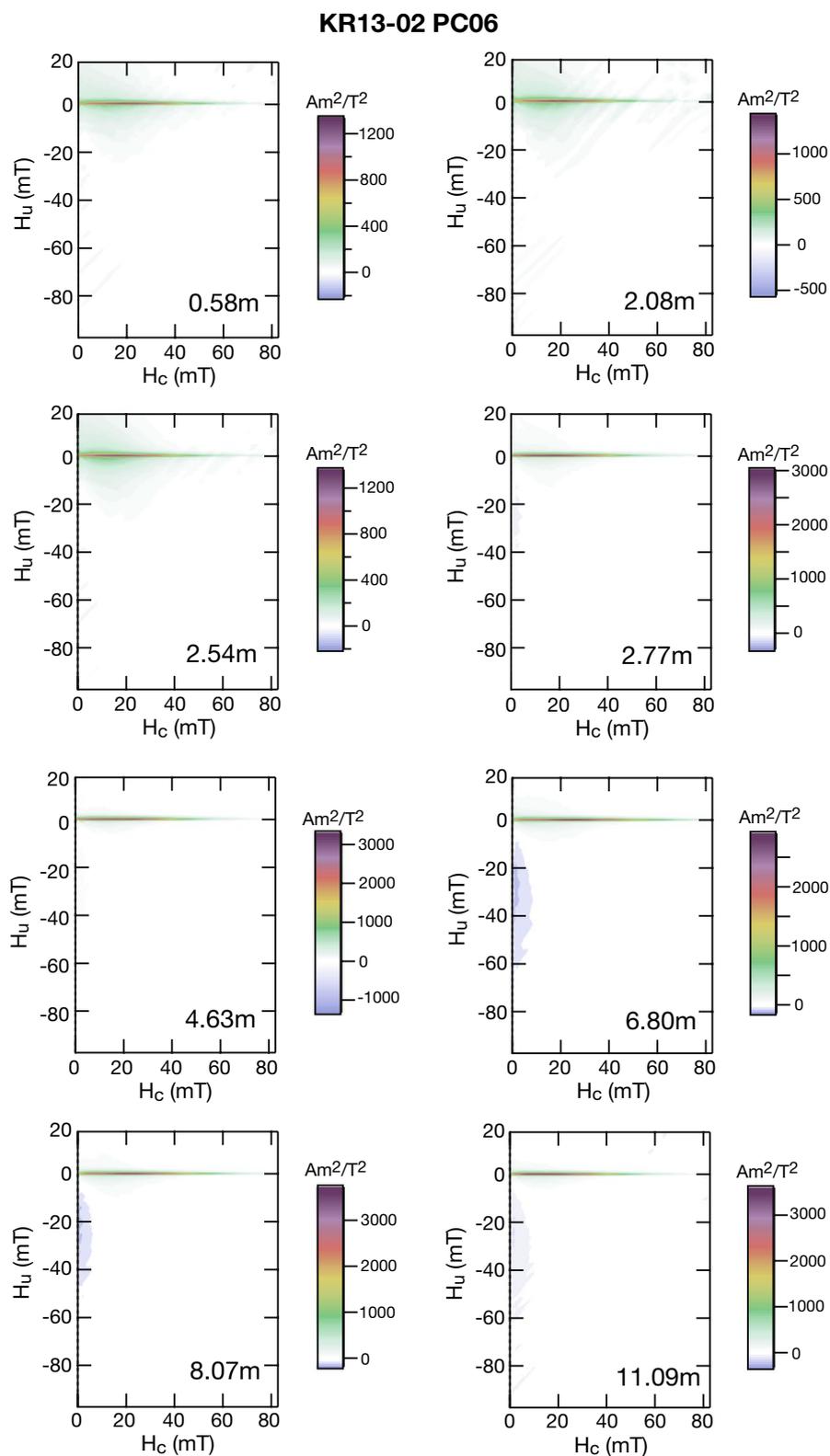
Fig. 3 Examples of FORC diagrams measured on samples from core KR13-02 PC06, western North Pacific Ocean

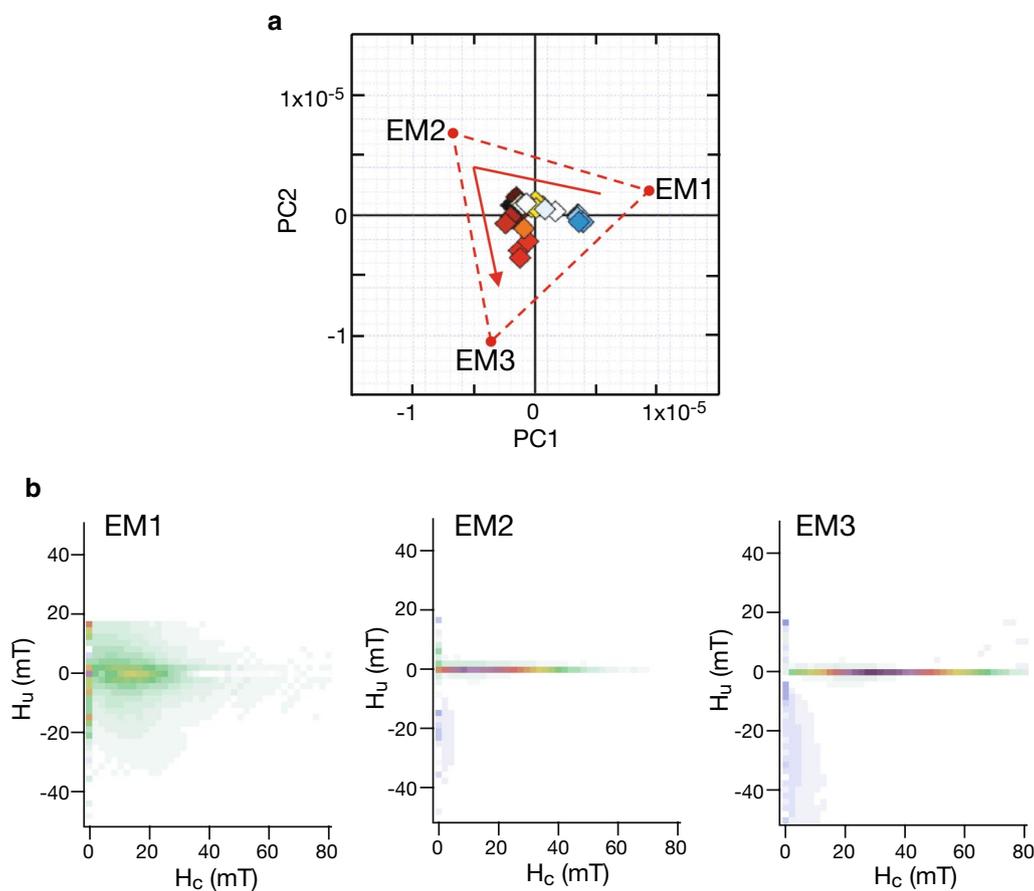Yamazaki *et al. Earth, Planets and Space*   (2020) 72:120

Page 7 of 15

Fig. 4 Principal component analysis (PCA) of first-order reversal curve (FORC) diagrams for core KR13-02 PC06. **a** Distribution of 26 FORC data (squares) on the principal component PC1-PC2 plane. Triangular dashed lines define a three-endmember (EM) system, and the arrow indicates the general downcore trend. **b** FORC diagrams for EM1, EM2, and EM3

are abundant throughout the core (Fig. 6a, b). The proportion of bullet-shaped magnetofossils is larger in the depth interval with a larger proportion of EM3 (Fig. 6b, d). Conversely, equant magnetofossils dominate magnetic extracts from other depths (Fig. 6a, c). We, thus, conclude that EM3 is carried by anisotropic biogenic magnetite particles (bullet shape and elongated), and EM2 is carried by equant biogenic magnetite particles with mainly octahedral morphology. The different shape anisotropy of the different magnetofossil morphologies is the likely cause of the coercivity differences between EM2 and EM3 (Berndt et al. 2020). EM2 and EM3 may correspond to the biogenic soft (BS) and biogenic hard (BH) components of Egli (2004a), which are defined based on coercivity component analyses of ARM/IRM acquisition/decay curves. However, the coercivities of EM2 and EM3 are lower than those of the BS and BH components of Egli (2004a), respectively. The cause of the difference is not clear, but it might be due to complete oxidization of magnetofossils under oxic conditions and to potentially

different axial ratios for bullet-shaped magnetofossils for EM3 (Ge et al. 2014; Usui et al. 2017).

Cores MR13E-02 Leg 2 PC01 and KR14-02 PC04, western North Pacific Ocean

FORC diagrams of samples from cores MR13-E02 Leg 2 PC01 and KR14-02 PC04 contain a central ridge that represents non-interacting biogenic SD grains and a broader component with large vertical spread, which is carried by interacting SD/vortex grains of presumably terrigenous origin (Additional file 1: Fig. S5). FORC distributions for all samples are almost the same as each other, which means that there is no significant magnetic mineral composition change either between the two cores or at different depths of each core. We analyzed data from the two cores together with those for core KR13-02 PC06 by FORC-PCA. As expected from the minor variability in FORC diagrams, the data points from the two cores form a tight cluster (Fig. 7), while those for core KR13-02 PC06 define a plane similar to the FORC-PCA results of core
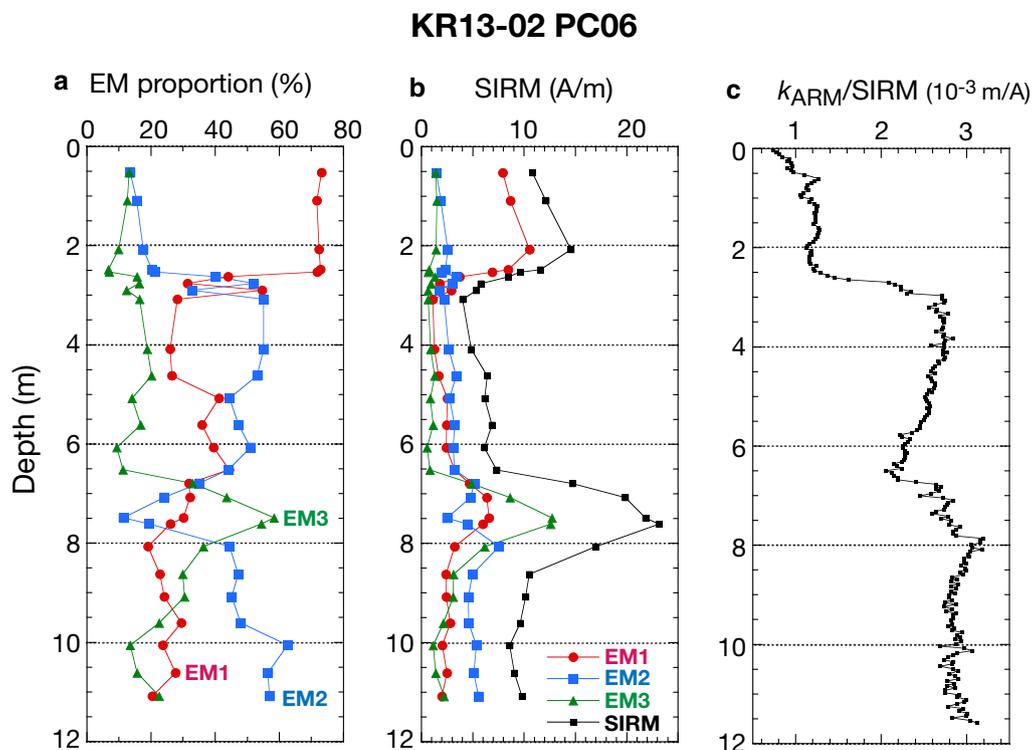
Yamazaki *et al. Earth, Planets and Space* (2020) 72:120

Page 8 of 15

Fig. 5 Downcore variations of FORC-PCA endmembers (EMs) and k_{ARM}/SIRM for core KR13-02 PC06. **a** The proportion of EM1 (red), EM2 (blue), and EM3 (green). **b** SIRM (black) and the contribution to SIRM of individual EMs calculated from the respective proportions. **c** Variations of k_{ARM}/SIRM. Note the synchronous changes of EMs and k_{ARM}/SIRM at ~ 2.7 m, and an EM3 increase between ~ 6.7 and 8.2 m

KR13-02 PC06 alone (Figs. 4, 7). Moreover, data points for the two cores are distributed near EM1-dominant samples of core KR13-02 PC06 (Fig. 7). This suggests that the magnetic mineral compositions of the two cores are similar through their entire depth to that above ~ 2.7 m of core KR13-02 PC06, where the terrigenous component dominates.

k_{ARM}/SIRM for cores MR13-E02 Leg 2 PC01 and KR14-02 PC04 ranges from ~ 0.3 to 0.6×10^{-3} m/A and ~ 0.9 to 1.5×10^{-3} m/A, respectively (Additional file 1: Figs. S2 and S3). These values are similar to those of core KR13-02 PC06 above ~ 2.7 m. This confirms the dominance of the terrigenous component in the former two cores.

IODP Hole U1365A, South Pacific Ocean
All 30 FORC diagrams for samples from Hole U1365A have a central ridge that represents the existence of biogenic magnetite intact chains (Additional file 1: Fig. S6), as reported by Yamazaki and Shimono (2013) and Shimono and Yamazaki (2016). Above ~ 8 m, a broader component with large vertical spread is also important in addition to the central ridge (Additional file 1: Fig. S6). From FORC-PCA, a two-EM system is defined in a single PC space (Fig. 8a). The data variance explained by the

single PC is not high, ~ 65%. However, adding PCs only increased slowly the variance explained. The arrow indicates a general downcore trend from near EM1 toward EM2. The FORC diagram for EM1 has an elliptical peak with a significant vertical spread (Fig. 8b). The outer contours diverge from the $H_u = 0$ axis, and elliptical closed contours peak at about $H_c = $ ~ 15 mT on the $H_u = 0$ axis. Another characteristic of EM1 is a peak close to the origin of the FORC diagram, which indicates the occurrence of superparamagnetic (SP) grains (Pike et al. 2001). We interpret EM1 as a terrigenous component constituting of a mixture of interacting SD/vortex and SP grains. The contribution of SP grains was not observed for the terrigenous component (EM1) of core KR13-02 PC06 from the western North Pacific. The representative FORC diagram for EM2, on the other hand, has a central ridge with no vertical spread and a small negative region near the vertical (H_u) axis below zero (Fig. 8b). We interpret this as a biogenic magnetite component. The coercivity distribution of EM2 at Hole U1365A is similar to that of the lower coercivity biogenic component (EM2) of core KR13-02 PC06 in the western North Pacific. Equant octahedra comprise the dominant magnetofossil morphology in Hole U1365A sediments (Yamazaki and Shimono
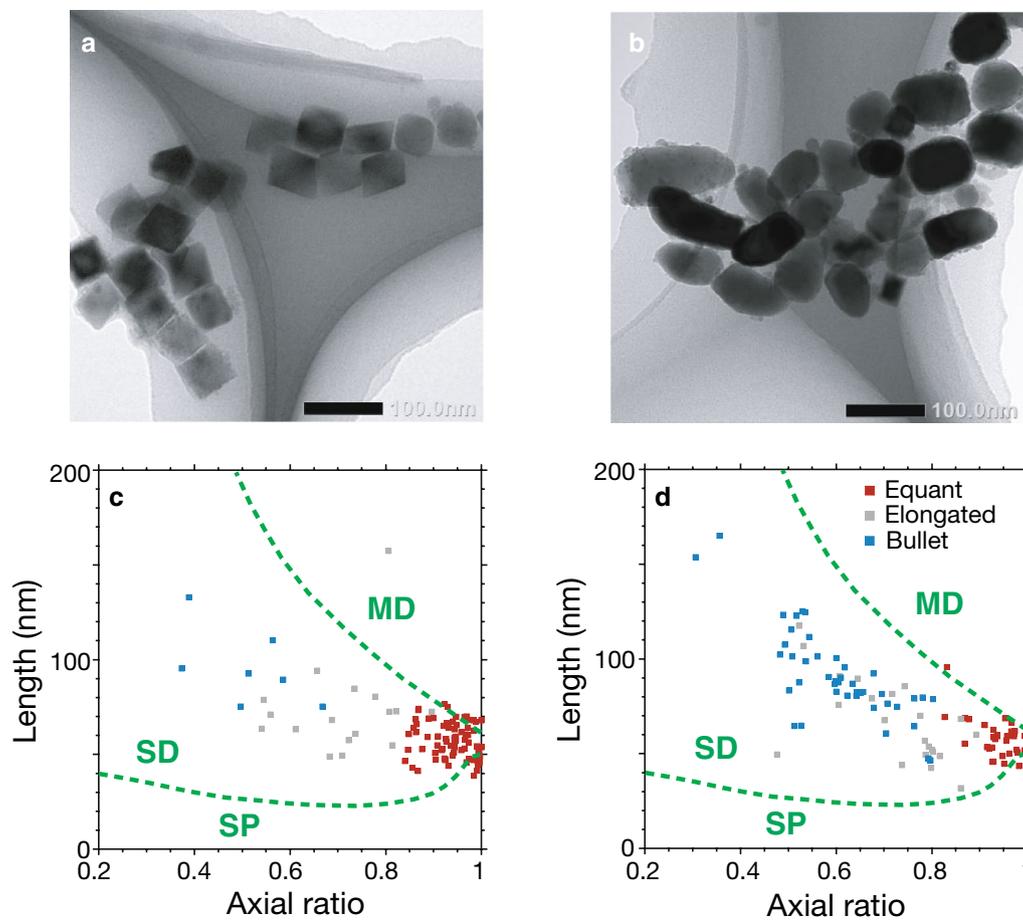
Yamazaki *et al. Earth, Planets and Space*   (2020) 72:120

Page 9 of 15

Fig. 6 Morphology of magnetofossils in core KR13-02 PC06. **a**, **b** TEM images of magnetic extracts from (**a**) 6.52 m and (**b**) 7.49 m. Scale bar: 100 nm. **c**, **d** Lengths and axial ratios of magnetofossils measured from TEM images at (**c**) 6.52 m and (**d**) 7.49 m. Magnetofossil morphology is classified into equant (red), elongated (gray), and bullet shaped (blue). SP, SD, and MD regions are after Tauxe et al. (2018)
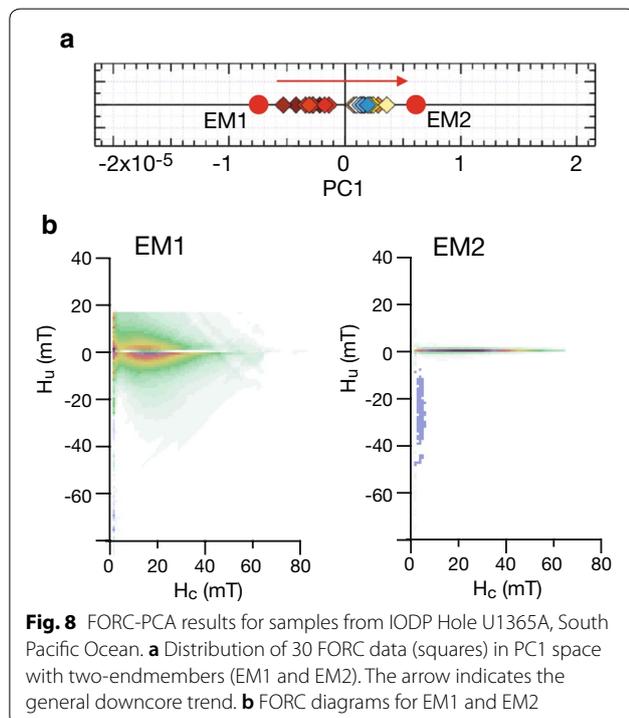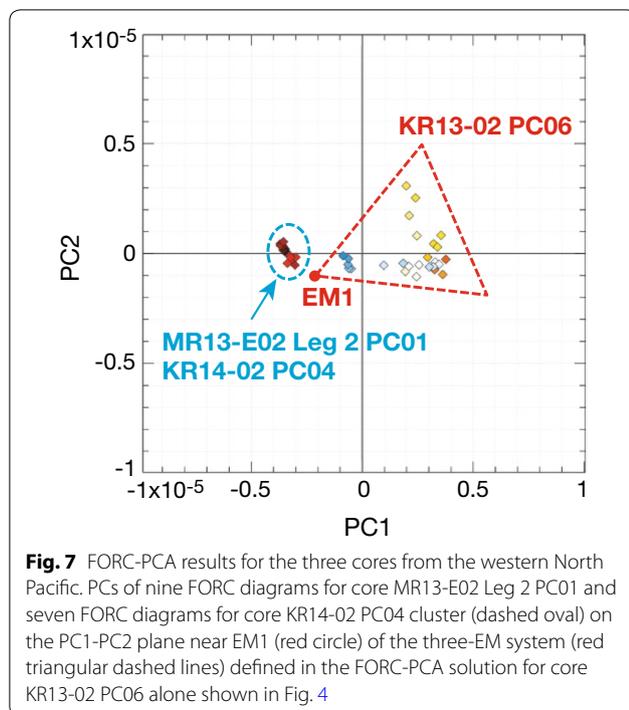
2013), which is consistent with the coercivity distribution of EM2.

Downcore variations in the proportion of the two EMs and the magnetization carried by them, which were calculated from the respective EM proportions and SIRM, are shown in Fig. 9 with k_{ARM}/SIRM variations (Shimono and Yamazaki 2016). The contribution of the terrigenous component (EM1) suddenly increases upward at ~8 m, which is accompanied by a k_{ARM}/SIRM drop. A gradual increase of the proportion of EM1 with depth below ~20 m is also accompanied by a k_{ARM}/SIRM decrease. These observations again confirm that the k_{ARM}/SIRM variations are due to changes in the proportion of biogenic to terrigenous magnetic components.

Discussion

In the western North Pacific Ocean, three EMs, a detrital (EM1) and two biogenic components with lower and higher coercivities (EM2 and EM3, respectively), were identified from FORC-PCA. The EM1 contribution increases abruptly upcore at ~2.7 m in core KR13-02 PC06, where the contributions of EM2 and EM3 to SIRM do not undergo significant changes. Consistency between the results of FORC-PCA and k_{ARM}/SIRM confirms that k_{ARM}/SIRM is a proxy for the proportion of biogenic to terrigenous magnetic components. The horizon in which the terrigenous component increases is close to the boundary between chemostratigraphical Units II and III, and its age is estimated to be around the E/O boundary (Fig. 2) (Ohta et al. 2020; Tanaka et al. 2020). FORC distributions for samples from cores MR13-E02 Leg 2 PC01 and KR14-02 PC04 indicate that magnetic mineral compositions are similar to those of core KR13-02 PC06 above ~2.7 m, and the ages of the former two cores are estimated to be Quaternary and Oligocene to Miocene, respectively. This suggests that the enhanced eolian input around the E/O boundary has continued through the Oligocene to Quaternary.
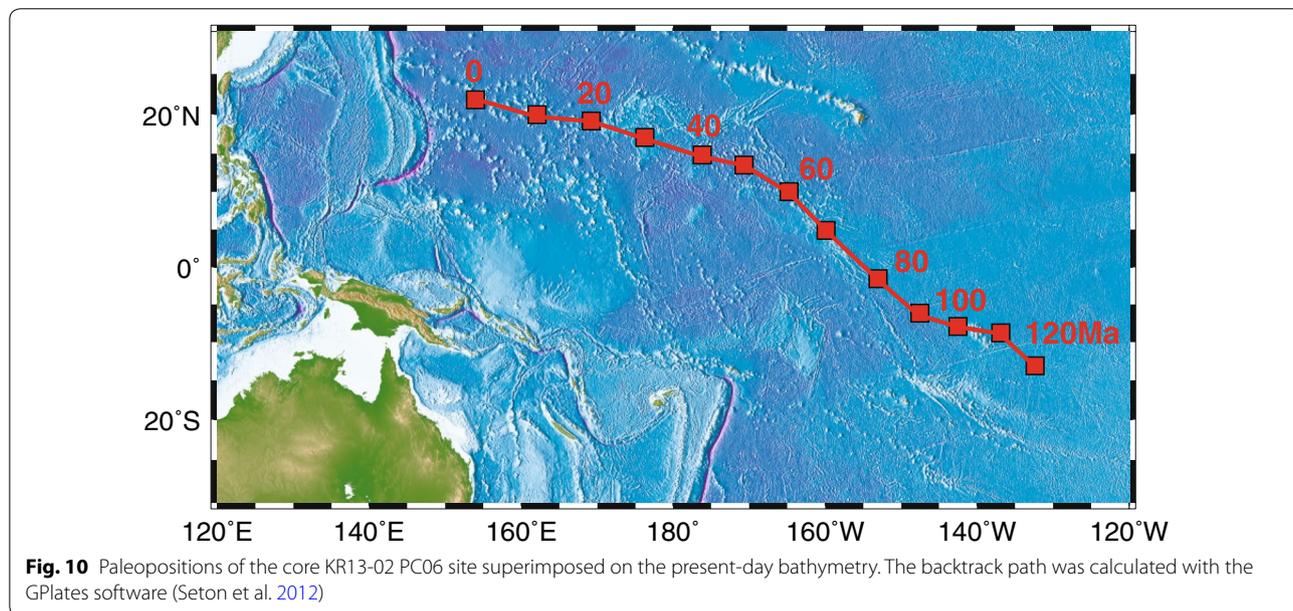
Fig. 7 FORC-PCA results for the three cores from the western North Pacific. PCs of nine FORC diagrams for core MR13-E02 Leg 2 PC01 and seven FORC diagrams for core KR14-02 PC04 cluster (dashed oval) on the PC1-PC2 plane near EM1 (red circle) of the three-EM system (red triangular dashed lines) defined in the FORC-PCA solution for core KR13-02 PC06 alone shown in Fig. 4

Fig. 8 FORC-PCA results for samples from IODP Hole U1365A, South Pacific Ocean. **a** Distribution of 30 FORC data (squares) in PC1 space with two-endmembers (EM1 and EM2). The arrow indicates the general downcore trend. **b** FORC diagrams for EM1 and EM2
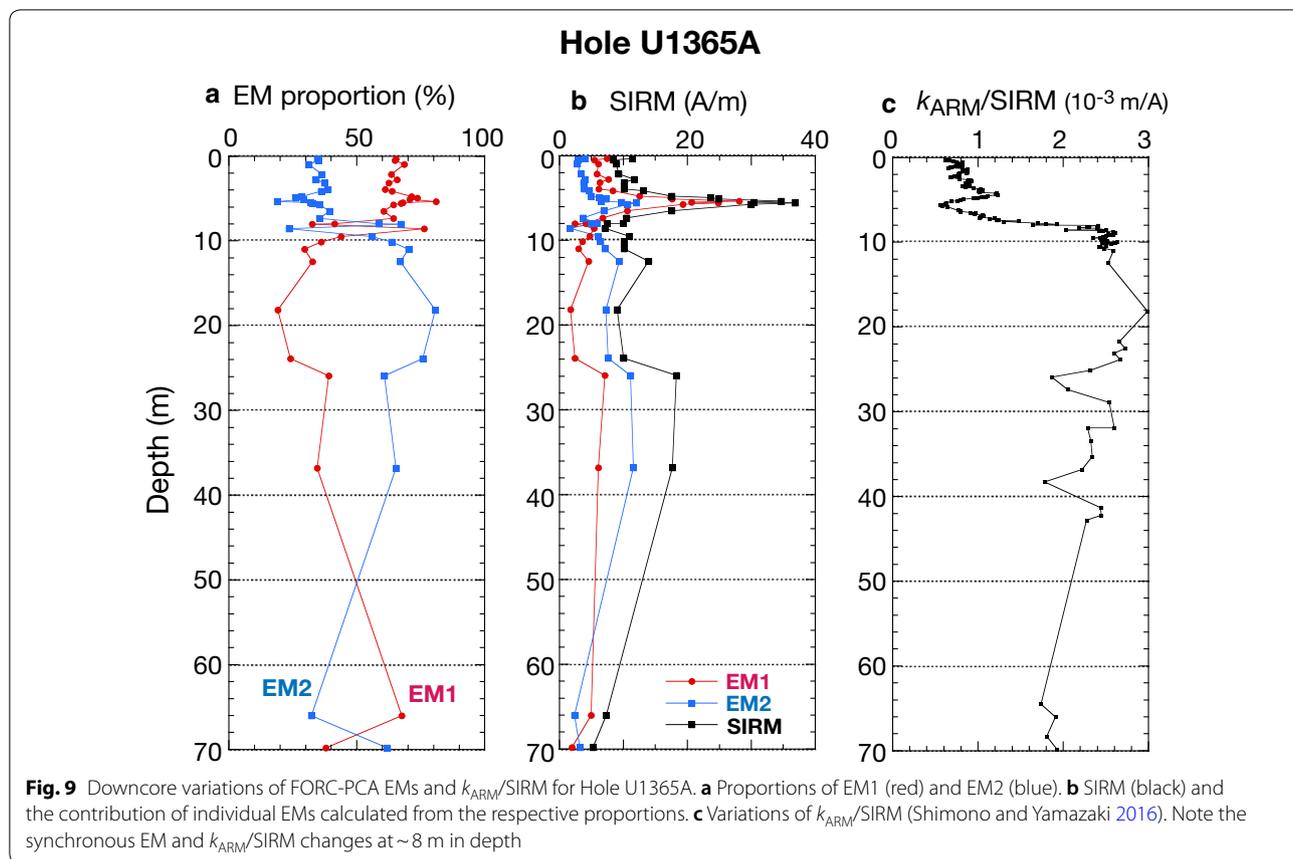
An increased terrigenous component also occurred in the South Pacific Ocean. FORC-PCA of Hole U1365A sediments identified terrigenous and biogenic EMs, and the terrigenous contribution increases upcore at ~8 m.

This result supports the previous rock-magnetic study of Hole U1365A by Shimono and Yamazaki (2016), which was based mainly on IRM component analyses and k_{ARM}/SIRM. The age of the increase at ~8 m is estimated to be around the E/O boundary (Additional file 1: Fig. S4). The terrigenous component of Hole U1365A includes ultrafine SP grains, which is not obvious in the western North Pacific cores. The difference in the grain-size distributions would reflect differences in the sources of detrital components and transportation processes between the western North Pacific and South Pacific Oceans.

The terrigenous component increases observed in core KR13-02 PC06 from the western North Pacific and Hole U1365A in the South Pacific may be due to tectonic drift of the two sites with Pacific plate motion into the regions influenced by the northern and southern hemisphere westerlies, respectively. It is known that eolian dust from arid Asian continental regions is the major source of terrigenous material to the North Pacific (Rex and Goldberg 1958; Blank et al. 1985), and a significant eolian dust flux increase occurs at around 20° N latitude and north at present (Rea et al. 1994; Uematsu et al. 2003; Mahowald et al. 2005). In addition, Yamazaki and Ioka (1997) reported that the proportion of high-coercivity magnetic minerals like hematite and goethite of presumably terrigenous origin increases between ~15 °N and 20 °N in surface sediments in a transect along 175° E longitude. Movement of the core KR13-02 PC06 site calculated with the GPlates software (Seton et al. 2012) is consistent with the scenario of entering a high eolian flux region; the site was located at ~16° N at the estimated age of the terrigenous increase, ~35 Ma (Fig. 10). For South Pacific Hole U1365A, the eolian dust source is considered to be Australia, which has the widest arid and semiarid areas in the southern hemisphere and is located windward of the site (Li et al. 2008; Stancin et al. 2008; Dunlea et al. 2015; Usui et al. 2018). Shimono and Yamazaki (2016) interpreted the terrigenous component increase at Hole U1365A as due to northward drift of Australia and the site to an arid middle latitude region in the Oligocene to Miocene.

Alternatively, the terrigenous increases in both the western North Pacific and South Pacific may represent a global cooling event. Eolian deposition in the ocean is controlled by global climate, including precipitation in eolian source regions and atmospheric circulation intensity (e.g., Rea 1994; Zhang et al. 2020). It is well documented that eolian dust flux increased since ~3 Ma in the North Pacific in response to northern hemisphere cooling (Rea 1994; Rea et al. 1998). Within the uncertainty of the age estimations of the red clay cores, the terrigenous increases recorded in both the western North Pacific and South Pacific may be coeval, and hence related to a single

Yamazaki *et al. Earth, Planets and Space* (2020) 72:120

Page 11 of 15

Fig. 9 Downcore variations of FORC-PCA EMs and k_{ARM}/SIRM for Hole U1365A. **a** Proportions of EM1 (red) and EM2 (blue). **b** SIRM (black) and the contribution of individual EMs calculated from the respective proportions. **c** Variations of k_{ARM}/SIRM (Shimono and Yamazaki 2016). Note the synchronous EM and k_{ARM}/SIRM changes at ~8 m in depth

Fig. 10 Paleopositions of the core KR13-02 PC06 site superimposed on the present-day bathymetry. The backtrack path was calculated with the GPlates software (Seton et al. 2012)

global paleoclimatic event. A possible candidate for such an event would be global cooling at the E/O boundary (Zachos et al. 2001). Increased aridity and eolian deposition was reported to have occurred in the Asian continent at the E/O boundary (Dupont-Nivet et al. 2007; Li et al. 2018; Wasiljeff et al. 2020).

Yamazaki *et al. Earth, Planets and Space*   (2020) 72:120

Page 12 of 15

TEM observations of samples from core KR13-02 PC06 from the western North Pacific demonstrate that the proportion of bullet-shaped magnetofossils is larger in the ~ 6.7 to 8.2 m interval, where the contribution of EM3 is larger. Except for this interval, the dominant magnetofossil morphology in this core is equant octahedra, which is consistent with previous observations of sediments from oxic environments (Yamazaki and Shimono 2013; Sakuramoto et al. 2017; Yamazaki and Yamamoto 2018). Usui et al. (2017, 2019) also reported a depth interval with a higher proportion of bullet-shaped magnetofossils in another red clay core taken in the vicinity (core MR15-E01 Leg 2 PC12). The respective intervals of the two cores are commonly within Unit V (Fig. 2), although it is not known whether they are coeval. These results suggest that the predominance of bullet-shaped magnetofossils occurred widely in red clay of the western North Pacific.

Previous studies have suggested that biogenic magnetite morphology can be a paleoenvironmental indicator (Hesse 1994; Yamazaki and Kawahata 1998; Egli 2004b; Yamazaki and Ikehara 2012; Chang et al. 2018). Magnetofossils with equant octahedral morphology are ubiquitous in oxic sediments (Yamazaki and Ioka 1997; Yamazaki and Shimono 2013; Yamazaki and Horiuchi 2016; Sakuramoto et al. 2017; Usui et al. 2017; Yamazaki and Yamamoto 2018). On the other hand, Yamazaki et al. (2019) proposed that magnetotactic bacteria that produce bullet-shaped magnetosomes prefer chemical conditions within the OATZ. Thus, the depth interval of ~ 6.7 to 8.2 m would have been in the OATZ during deposition, although the studied red-clay core is now in oxic conditions throughout its entire depth. Biological productivity is higher near the equator than in middle latitudes, so the OATZ can be shallow in a sediment column near the equator. Hence, the dominance of bullet-shaped magnetofossils may be an indicator of the timing during which the site was in paleo-equatorial regions. According to the paleopositions calculated with the GPlates software (Seton et al. 2012), the core KR13-02 PC06 site was located within 5° latitude of the equator between ~ 70 and 85 Ma (Fig. 10).

Conclusions

Our rock-magnetic analyses and TEM observations of red-clay cores from the western North Pacific and at Hole U1365A in the South Pacific lead to the following conclusions.

1. Magnetic endmembers that represent terrigenous and biogenic components were identified by FORC-PCA unmixing. The terrigenous component, which is considered to be transported as eolian dust, suddenly increased in both hemispheres. The age of the increase is estimated to be around the E/O boundary. The terrigenous increase at the two sites may have resulted from tectonic drift of the sites with Pacific plate motion into regions influenced by the northern and southern hemisphere westerlies, respectively. Alternatively they may be related to global cooling at the E/O boundary.

2. Two biogenic EMs with different coercivity distributions were identified with FORC-PCA in the western North Pacific core. The higher coercivity EM has a higher proportion of bullet-shaped magnetofossils, and the contribution of this EM increases in a certain depth interval of the core. Although the core is now under oxic conditions throughout its entire depth, the sediments of this interval were in the OATZ, likely because the sediments were deposited within a high productivity equatorial zone. The increased abundance of bullet-shaped magnetofossils in red clay may be an indicator of its formerly paleo-equatorial position.

Supplementary information

Additional file 1: Fig. S1. Photos of three piston cores from the western North Pacific Ocean. **Fig. S2.** Inclination of remanent magnetization and k_{ARM}/SIRM for core MR13-E02 Leg 2 PC01. **Fig. S3.** Inclination of remanent magnetization and k_{ARM}/SIRM for core KR14-02 PC04. **Fig. S4**. Age estimation of IODP Hole U1365A sediments, South Pacific Ocean. **Fig. S5**. Examples of FORC diagrams for two cores from the western North Pacific Ocean. **Fig. S6**. Examples of FORC diagrams for IODP Hole U1365A, South Pacific Ocean.

Additional file 2. Data file for FORC-PCA endmembers, SIRM, and k_{ARM}/SIRM. Datasets of for KR13-02 PC06 and Hole U1365A are provided as separate sheets in the Excel file.

Yamazaki *et al. Earth, Planets and Space*   (2020) 72:120

Page 13 of 15

Authors' contributions
TY and YU designed the project. TY and WF wrote the manuscript. TY, YU, and TS collected samples. TY, WF, and TS conducted measurements and data analyses. All authors read and approved the final manuscript.

Availability of data and materials
The data presented in Figs. 5 and 9 are included in Additional file 2. The raw FORC data and TEM images are available from the corresponding author on request. Materials from the studied cores from the western North Pacific can be requested from JAMSTEC through the Data and Sample Research System for Whole Cruise Information (DARWIN), and Hole U1365A materials can be requested from IODP.

Ethics approval and consent to participate
Not applicable.

Consent for publication
Not applicable.

Competing interests
The authors declare that they have no competing interests.

Author details
[1] Atmosphere and Ocean Research Institute, The University of Tokyo, Kashiwa, Japan. [2] Geological Survey of Japan, National Institute of Advanced Industrial Science and Technology, Tsukuba, Japan. [3] Volcanoes and Earth's Interior Research Center, Research Institute of Marine Geodynamics, Japan Agency for Marine-Earth Science and Technology, Yokosuka, Japan.

References
Banerjee SK, King J, Marvin J (1981) A rapid method for magnetic granulometry with applications to environmental studies. Geophys Res Lett 8:333–336

Bazylinski DA, Frankel RB (2004) Magnetosome formation in prokaryotes. Nat Rev Microbiol 2:217–230

Berndt TA, Chang L, Pei Z (2020) Mind the gap: towards a biogenic magnetite paleoenvironmental proxy through an extensive finite-element micromagnetic simulation. Earth Planet Sci Lett 532:116010. https://doi.org/10.1016/j.epsl.2019.116010

Blakemore RP, Maratea D, Wolfe RS (1979) Isolation and pure culture of a freshwater magnetic spirillum in chemically defined medium. J Bacteriol 140:720–729

Blank M, Leinen M, Prospero JM (1985) major Asian aeolian inputs indicated by the mineralogy of aerosols and sediments in the western North Pacific. Nature 314:84–86

Chang L, Roberts AP, Winklhofer M, Heslop D, Dekkers MJ, Krigsman W, Fitz Gerald JD, Smith P (2014) Magnetic detection and characterization of biogenic magnetic minerals: a comparison of ferromagnetic resonance and first-order reversal curve diagrams. J Geophys Res Solid Earth 119:6136–6158

Chang L, Harrison RJ, Zeng F, Berndt TA, Roberts AP, Heslop D, Zhao X (2018) Coupled microbial bloom and oxygenation decline recorded by magnetofossils during the Palaeocene-Eocene thermal maximum. Nat Comm 9:4007. https://doi.org/10.1038/s41467-018-06472-y

Channell JET, Harrison RJ, Lascu I, McCave IN, Hibbert FD, Austin WEN (2016) Magnetic record of deglaciation using FORC-PCA, sortable-silt grain size, and magnetic excursion at 26 ka, from the Rockall Trough (NE Atlantic). Geochem Geophys Geosyst 17:1823–1841. https://doi.org/10.1002/2016GC006300

Chen AP, Egli R, Moskowitz BM (2007) First-order reversal curve (FORC) diagrams of natural and cultured biogenic magnetic particles. J Geophys Res. 112:B08S90. https://doi.org/10.1029/2006jb004575

D'Hondt S, Inagaki F, Zarikian AZ, Abrams LJ, Subois N, Engelhardt T, Evans H, Ferdelman T, Gribsholt B, Harris RN, Hoppie BW, Hyun JH, Kallmeyer J, Kim J, Lynch JE, McKinley CC, Mitsunobu S, Morono Y, Murray RW, Pockalny R, Sauvage J, Shimono T, Shiraishi F, Smith DC, Smith-Duque CE, Spivack AJ, Olav Steinsbu B, Suzuki Y, Szpak M, Toffin L, Uramoto G, Yamaguchi YT, Zhang GL, Zhang XH, Ziebis W (2015) Presence of oxygen and aerobic communities from sea floor to basement in deep-sea sediments. Nat Geosci 8:299–304

Data and Sample Research System for Whole Cruise Information (DARWIN) (2020) Japan Agency for Marine-Earth Science and Technology, Yokosuka. http://www.godac.jamstec.go.jp/darwin/e. Accessed 23 April 2020

Doh SJ, King JW, Leinen M (1988) A rock-magnetic study of giant piston core LL44-GPC3 form the central north Pacific and its paleoceanographic implications. Paleoceanography 3:89–111

Dunlea AG, Murray RW, Sauvage J, Spivack AJ, Harris RN, D'Hondt S (2015) Dust, volcanic ash, and the evolution of the South Pacific Gyre through the Cenozoic. Paleoceanography 30:1078–1099

Dupont-Nivet G, Krigsman W, Langereis CG, Abels HA, Dai S, Fang X (2007) Tibetan plateau aridification linked to global cooling at the Eocene-Oligocene transition. Nature 445:635–638

Egli R (2004a) Characterization of individual rock magnetic components by analysis of remanence curves. 2. Fundamental properties of coercivity distributions. Phys Chem Earth 29:851–867

Egli R (2004b) Characterization of individual rock magnetic components by analysis of remanence curves. 3. Bacterial magnetite and natural processes in lakes. Phys Chem Earth 29:869–884

Egli R (2013) VARIFORC: an optimized protocol for calculating non-regular first-order reversal curve (FORC) diagrams. Glob Planet Change 110:302–320

Egli R, Chen AP, Winklhofer M, Kodama KP, Horng CS (2010) Detection of noninteracting single domain particles using first-order reversal curve diagrams. Geochem Geophys Geosyst 11:Q01Z11. https://doi.org/10.1029/2009gc002916

Expedition 329 Scientists (2011) Site U1365. In: D'Hondt S, Inagaki F, Alvarez Zarikian CA, the Expedition 329 Scientists (eds) Proceedings of IODP, vol. 329. Integrated Ocean Drill Program Manage Int Inc, Tokyo. https://doi.org/10.2204/iodp.proc.329.103.2011

Fujinaga K, Yasukawa K, Nakamura K, Machida S, Takaya Y, Ohta J, Araki S, Liu H, Usami R, Maki R, Haraguchi S, Nishio Y, Usui Y, Nozaki T, Yamazaki T, Ichiyama Y, Ijiri A, Inagaki F, Machiyama H, Iijima K, Suzuki K, Kato Y (2016) KR13-02, MR13-E02 Leg 2 and KR14-02 Cruise members, Geochemistry of REY-rich mud in the Japanese Exclusive Economic Zone around Minami-torishima Island. Geochem J 50:575–590

Ge K, Williams W, Liu Q, Yu Y (2014) Effects of the core-shell structure on the magnetic properties of partially oxidized magnetite grains: experimental and micromagnetic investigations. Geochem Geophys Geosyst 15:2021–2038

Harrison RJ, Feinberg JM (2008) FORCinel: an improved algorithm for calculating first-order reversal curve distributions using locally weighted regression smoothing. Geochem Geophys Geosyst 9:Q05016. https://doi.org/10.1029/2008GC001987

Harrison RJ, Lascu I (2014) FORCulator: a micromagnetic tool for simulating first-order reversal curve diagrams. Geochem Geophys Geosyst 15:4671–4691

Harrison RJ, Muraszko J, Heslop D, Lascu I, Muxworthy AR, Roberts AP (2018) An improved algorithm for unmixing first-order reversal curve diagrams using principal component analysis. Geochem Geophys Geosyst 19:1595–1610

Hesse PP (1994) Evidence for bacterial palaeoecological origin of mineral magnetic cycles in oxic and sub-oxic Tasman Sea sediments. Mar Geol 117:1–17

Hovan SA, Rea DK, Pisias NG (1991) Late Pleistocene continental climate and oceanic variability recorded in northwest Pacific sediments. Paleoceanography 6:349–370

Iijima K, Yasukawa K, Fujinaga K, Nakamura K, Machida S, Takaya Y, Ohta J, Haraguchi S, Nishio Y, Usui Y, Nozaki T, Yamazaki T, Ichiyama Y, Ijiri A, Inagaki F, Machiyama H, Suzuki S, Kato Y (2016) KR13-02 Cruise members, Discovery of extremely REY-rich mud in the western North Pacific Ocean. Geochem J 50:557–573

Janecek TR, Rea DK (1983) Eolian deposition in the northeast Pacific Ocean: Cenozoic history of atmospheric circulation. Geol Soc Amer Bull 94:730–738

Yamazaki *et al. Earth, Planets and Space* (2020) 72:120

Page 14 of 15

Kato Y, Fujinaga K, Nakamura K, Takaya Y, Kitamura K, Ohta J, Toda R, Nakashima T, Iwamori H (2011) Deep-sea mud in the Pacific Ocean as a potential resource for rare-earth elements. Nat Geosci 4:535–539

King J, Banerjee SK, Marvin J, Özdemir Ö (1982) A comparison of different magnetic methods for determining the relative grain size of magnetite in natural materials: some results from lake sediments. Earth Planet Sci Lett 59:404–419

Kopp RE, Kirschvink JL (2008) The identification and biogeochemical interpreta-tion of fossil magnetotactic bacteria. Earth-Sci Rev 86:42–61

Lascu I, Harrison RJ, Li Y, Muraszko JR, Channell JET, Piotrowski AM, Hodell DA (2015) Magnetic unmixing of first-order reversal curve diagrams using principal component analysis. Geochem Geophys Geosyst 16:2900–2915

Lefèvre CT, Bazylinski DA (2013) Ecology, diversity, and evolution of magneto-tactic bacteria. Microbiol Mol Biol Rev 77:497–526

Li F, Ginoux P, Ramaswamy V (2008) Distribution, transport, and deposition of mineral dust in the Southern Ocean and Antarctica: contribution of major sources. J Geophys Res 113:D10207. https://doi.org/10.1029/2007J D009190

Li J, Wu W, Liu Q, Pan Y (2012) Magnetic anisotropy, magnetostatic interac-tions and identification of magnetofossils. Geochem Geophys Geosyst 13:Q10Z51. https://doi.org/10.1029/2012gc004384

Li JX, Yue LP, Roberts AP, Hirt AM, Pan F, Guo L, Xu Y, Xi RG, Guo L, Qiang XK, Gai CC, Jiang ZX, Sun ZM, Liu QS (2018) Global cooling and enhanced Eocene Asian mid-latitude interior aridity. Nat Com 9:3026. https://doi.org/10.1038/s41467-018-05415-x

Liu Q, Roberts AP, Larrasoaña JC, Banerjee SK, Guyodo Y, Tauxe L, Oldfield F (2012) Environmental magnetism: principles and applications. Rev Geophys 50:4002. https://doi.org/10.1029/2012rg000393

Mahowald MM, Baker AR, Bergametti G, Brooks N, Duce RA, Jickells TD, Kubilay N, Prospero JM, Tegan I (2005) Atmospheric global dust cycle and iron inputs to the ocean. Global Biochem Cy 19:GB4025. https://doi.org/10.1029/2004gb002402

Muxworthy AR, Heslop D, Williams W (2004) Influence of magnetostatic inter-actions on first-order-reversal-curve (FORC) diagrams: a micromagnetic approach. Geophys J Int 158:888–897

Muxworthy AR, King JG, Heslop D (2005) Assessing the ability of first-order reversal curve (FORC) diagrams to unravel complex magnetic signals. J Geophys Res 110:B01105. https://doi.org/10.1029/2004JB003195

Newell AJ (2005) A high-precision model of first-order reversal curve (FORC) functions for single-domain ferromagnets with uniaxial anisotropy. Geochem Geophys Geosyst 6:Q05010. https://doi.org/10.1029/2004G C000877

Nozaki T, Ohta J, Noguchi T, Sato H, Ishikawa A, Takaya Y, Kimura JI, Chang Q, Shimada K, Ishibashi J, Yasukawa K, Kimoto K, Iijima K, Kato Y (2019) A Miocene impact ejecta layer in the pelagic Pacific Ocean. Sci Rep 9:16111. https://doi.org/10.1038/s41598-019-52709-1

Ohta J, Yasukawa K, Nozaki T, Takaya Y, Mimura K, Fujinaga K, Nakamura K, Usui Y, Kimura J-I, Chang Q, Kato Y (2020) Fish proliferation and rare-earth dep-osition by topographically induced upwelling at the late Eocene cooling event. Sci Rept 10:9896. https://doi.org/10.1038/s41598-020-66835-8

Opdyke ND, Foster JH (1970) Paleomagnetism of cores from the North Pacific. Geol Soc Amer Memoir 126:83–119

Pike CR, Roberts AP, Verosub KL (1999) Characterizing interactions in fine magnetic particle systems using first order reversal curves. J Appl Phys 85:6660–6667

Pike CR, Roberts AP, Verosub KL (2001) First-order reversal curve diagrams and thermal relaxation effects in magnetic particles. Geophys J Int 145:721–730

Rea DK (1994) The paleoclimatic record provided by eolian deposition in the deep sea: the geologic history of wind. Rev Geophys 32:159–195

Rea DK, Hovan S, Janecek TR (1994) Late Quaternary flux of eolian dust to the Pacific Ocean. In: Hay WW (ed) Material fluxes on the surface of the Earth. National Academy Press, Washington DC, pp 116–124

Rea DK, Snoeckx H, Joseph LH (1998) Late Cenozoic eolian distribution in the North Pacific: Asian drying, Tibetan uplift, and cooling of the northern hemisphere. Paleoceanography 13:215–224

Rex RW, Goldberg ED (1958) Quartz Contents of Pelagic Sediments of the Pacific Ocean. Tellus 10:153–159

Roberts AP, Pike CR, Verosub KL (2000) First-order reversal curve diagrams: a new tool for characterizing the magnetic properties of natural samples. J Geophys Res 105:28461–28475

Roberts AP, Florindo F, Villa G, Chang L, Jovane L, Bohaty SM, Larrasoaña JC, Heslop D, Fitz Gerald JD (2011) Magnetotactic bacterial abundance in pelagic marine environments is limited by organic carbon flux and avail-ability of dissolved iron. Earth Planet Sci Lett 310:441–452

Roberts AP, Chang L, Heslop D, Florindo F, Larrasoaña JC (2012) Searching for single domain magnetite in the "pseudo-single domain" sedimentary haystack: implications of biogenic magnetite preservation for sediment magnetism and relative paleointensity determinations. J Geophys Res 117:B08104. https://doi.org/10.1029/2012JB009412

Roberts AP, Florindo F, Chang L, Heslop D, Jovane L, Larrasoaña JC (2013) Mag-netic properties of pelagic marine carbonate. Earth-Sci Rev 127:111–139

Roberts AP, Heslop D, Zhao X, Pike CR (2014) Understanding fine magnetic particle systems through use of first-order reversal curve diagrams. Rev Geophys 53:557–602. https://doi.org/10.1002/2014RG000462

Roberts AP, Zhao X, Harrison RJ, Heslop D, Muxworthy AR, Rowan CJ, Larra-soaña JC, Florindo F (2018) Signatures of reductive magnetic mineral diagenesis from unmixing of first-order reversal curves. J Geophys Res Solid Earth 123:4500–4522. https://doi.org/10.1029/2018JB015706

Sakuramoto Y, Yamazaki T, Kimoto K, Miyairi Y, Kuroda J, Yokoyama Y, Matsuzaki H (2017) A geomagnetic paleointensity record of 0.6 to 3.2 Ma from sediments in the western equatorial Pacific and remanent magnetization lock-In depth. J Geophys Res Solid Earth 122:7525–7543

Seton M, Müller RD, Zahirovic S, Gaina C, Torsvik T, Shephard G, Talsma A, Gur-nis M, Turner M, Maus S, Chandler M (2012) Global continental and ocean basin reconstructions since 200 Ma. Earth-Sci Rev 113:212–270

Shimono T, Yamazaki T (2016) Environmental rock magnetism of Cenozoic red clay in the South Pacific. Geochem Geophys Geosyst 17:1296–1311

Stancin AM, Gleason JD, Hovan SA, Rea DK, Owen RM, Moore TC Jr, Hall CM, Blum JD (2008) Miocene to recent eolian dust record from the Southwest Pacific Ocean at 40° S latitude. Palaeogeogr Palaeoclimatol Palaeoecol 261:218–233

Tanaka E, Nakamura K, Yasukawa K, Miura K, Fujinaga K, Iijima K, Nozaki T, Kato Y (2020) Chemostratigraphy of deep-sea sediments in the western North Pacific Ocean: implications for genesis of mud highly enriched in rare-earth elements and yttrium. Ore Geol Rev 119:103392. https://doi.org/10.1016/j.oregeorev.2020.103392

Tauxe L, Banerjee SK, Butler RF, van der Voo R (2018) Essentials of paleomag-netism. 5th Web Edition. https://earthref.org/MagIC/books/Tauxe/Essen tials/

Thompson R, Oldfield F (1986) Environmental magnetism. Allen and Unwin, London

Uematsu M, Wang Z, Uno I (2003) Atmospheric input of mineral dust to the western North Pacific region based on direct measurements and a regional chemical transport model. Geophys Res Lett 30:1342. https://doi.org/10.1029/2002GL016645

Usui Y, Yamazaki T, Saitoh M (2017) Changing abundance of magnetofossil morphologies in pelagic red clay around Minamitorishima, western North Pacific. Geochem Geophys Geosyst 18:4558–4572

Usui Y, Shimono T, Yamazaki T (2018) Rock magnetism of quartz and feldspars chemically separated from pelagic red clay: a new approach to prov-enance study. Earth Planets Space 70:133. https://doi.org/10.1186/s4062 3-018-0918-1

Usui Y, Yamazaki T, Oka T, Kumagai Y (2019) Inverse magnetic susceptibility fabrics in pelagic sediment: implications for magnetofossil abundance and alignment. J Geophys Res Solid Earth 124:10672–10686

Wasiljeff J, Kaakinen A, Salminen JM, Zhang Z (2020) Magnetostratigraphic constraints on the fossiliferous Ulantatal sequence in Inner Mongolia, China: implications for Asian aridification and faunal turnover before the Eocene-Oligocene boundary. Earth Planet Sci Lett 535:116125. https://doi.org/10.1016/j.epsl.2020.116125

Yamazaki T (2008) Magnetostatic interactions in deep-sea sediments inferred from first-order reversal curve diagrams: implications for relative paleoin-tensity normalization. Geochem Geophys Geosyst 9:Q02005. https://doi.org/10.1029/2007GC001797

Yamazaki T, Horiuchi K (2016) Precessional control on ocean productivity in the Western Pacific Warm Pool for the last 400 kyr: insight from biogenic magnetite. Geochem Geophys Geosyst 17:4399–4412

Yamazaki T, Ikehara M (2012) Origin of magnetic mineral concentration vari-ation in the Southern Ocean. Paleoceanography PA27:2206. https://doi.org/10.1029/2011pa002271

Yamazaki *et al. Earth, Planets and Space*   (2020) 72:120

Page 15 of 15

Yamazaki T, Ioka N (1997) Environmental rock-magnetism of pelagic clay: implications for Asian eolian input to the North Pacific since the Pliocene. Paleoceanography 12:111–124

Yamazaki T, Kawahata H (1998) Organic carbon flux controls the morphology of magnetofossils in marine sediments. Geology 26:1064–1066

Yamazaki T, Shimono T (2013) Abundant bacterial magnetite occurrence in oxic red clay. Geology 41:1191–1194

Yamazaki T, Yamamoto Y (2018) Relative paleointensity and inclination anomaly over the last 8 Myr obtained from the Integrated Ocean Drilling Program Site U1335 sediments in the eastern equatorial Pacific. J Geophys Res Solid Earth 123:7305–7320

Yamazaki T, Yamamoto Y, Acton G, Guidry EP, Richter C (2013) Rock-magnetic artifacts on long-term relative paleointensity variations in sediments. Geochem Geophys Geosyst 14:29–43. https://doi.org/10.1029/2012GC004546

Yamazaki T, Suzuki Y, Kouduka M, Kawamura N (2019) Dependence of bacterial magnetosome morphology on chemical conditions in deep-sea sediments. Earth Planet Sci Lett 513:135–143

Zachos J, Pagani M, Sloan L, Thomas E, Billups K (2001) Trends, rhythms, and aberrations in global climate 65 Ma to present. Science 292:686–693

Zhang Q, Liu Q, Li J, Sun Y (2018) An integrated study of the eolian dust in pelagic sediments from the North Pacific Ocean based on environmental magnetism, transmission electron microscopy, and diffuse reflectance spectroscopy. J Geophys Res Solid Earth 123:3358–3376

Zhang Q, Liu Q, Roberts AP, Larrasoaña JC, Shi X, Jin C (2020) Mechanism for enhanced eolian dust flux recorded in North Pacific Ocean sediments since 4.0 Ma: aridity or humidity at dust source areas in the Asian interior? Geology 48:77–81